Aerodynamic Characteristics of Ducted Propulsion Fan Using Secondary Air Intake

Thai-Son Vu , Binh-Nguyen Nguyen , Hoang-Quan Chu , Gia-Diem Pham , Cong Truong Dinh *

Posted Date: 27 April 2026

doi: 10.20944/preprints202604.1792.v1

Keywords: electric vertical take-off and landing; electric ducted propulsion fan (eDPF); secondary air intake channel; RANS analysis; flow phenomena; thrust; torque

 doi:10.20944/preprints202604.1792.v1

Article

Aerodynamic Characteristics of Ducted Propulsion Fan Using Secondary Air Intake

Thai-Son Vu [1], Binh-Nguyen Nguyen [1], Hoang-Quan Chu [2], Gia-Diem Pham [1] and Cong Truong Dinh [1,*]

[1] School of Mechanical Engineering, Hanoi University of Science and Technology, No 1, Dai Co Viet street, Bach Mai Ward, Hanoi 11615, Vietnam

[2] Le Quy Don Technical University, 236, Hoang Quoc Viet street, Hanoi 11917, Vietnam

* Correspondence: truong.dinhcong@hust.edu.vn

Abstract

Today, the aviation industry is transitioning from fossil fuel to renewable energy. Renewable energy systems have advantages, such as cleanliness and reduced emissions, but also face limitations in battery energy density and aerodynamic performance during operation. Therefore, electric ducted propulsion fans (eDPFs) are a promising solution that uses duct components to enhance aerodynamic efficiency and operational safety. This study utilizes average Navier-Stokes analysis, incorporating Reynolds numbers and a k-ω SST turbulence model, to examine eDPF configurations both with and without a secondary air intake channel, concentrating on internal flow dynamics and aerodynamic efficiency. The air intake channel, which is located close to the tip of the rotor blade, helps the eDPF move more mass and create more thrust. Several different configurations of the secondary air intake channel were tested by varying the intake channel position, curvature, and size of the inlet and outlet ports under static conditions at 6000 rpm. The best design improved thrust by an additional 2.2% compared to the baseline case without the auxiliary intake port.

Keywords: electric vertical take-off and landing; electric ducted propulsion fan (eDPF); secondary air intake channel; RANS analysis; flow phenomena; thrust; torque

1. Introduction

Electric propulsion ducted fans (eDPFs) have become the great propulsion system for small to medium-sized airborne platforms, particularly in unmanned aerial vehicles (UAVs), personal airborne mobility vehicles (PAMs), and electric vertical take-off and landing (eVTOL) aircraft. The aerodynamically enclosed structure of the eDPF provides safety, compactness, and great static thrust compared to open-type propellers. Abrego and Bulaga [1] make an experimental study of the guide configuration that enhances axial and forward flight performance due to the interaction between the lift generated by the guide, the rotor thrust, and the pressure recovery at the guide's outlet. While the guide contributes to enhanced thrust, its aerodynamic behavior is complex and influenced by many interdependent parameters, including wingtip clearance, inlet flow deformation, guide shape, and rotor-encase interaction.

The vortex caused by blade tip leakage leads to aerodynamic loss of eDPF. The different pressure on the blade tip creates these vortices, creates a swirling flow structure, and disrupts the wake field. This not only reduces effective pressure gain but also causes turbulence and acoustic emission. In axial compressors, similar problems with blade tip leakage have been widely studied. Dinh et al. [2] study the casing groove and blade tip injection to control blade tip leakage flow in supersonic axial compressors; their results showed that these modifications altered the pressure field at the vane tip, thus slowing down flow separation and stabilizing flow. By creating controlled vortex disruption through casing groove modification, the compressor achieved improved stall margin and total

 doi:10.20944/preprints202604.1792.v1

pressure ratio—mechanisms that could be directly transferred to EDF designs under similar operating conditions.

Another way to control blade tip leakage is the rotor bleeding method. This method makes a secondary airflow at the rotor blade tip to prevent vortex formation. Unlike blade tip injection, which requires additional mass flow rate, rotor bleeding can be performed passively with appropriate geometry. Dinh et al. [3] study the structural and aerodynamic benefits of rotor bleeding airflow, including reduced blade tip leakage vortex and improved pressure recovery. Vu et al. [4] successfully applied this bleeding method to eDPF. Their numerical simulations, based on the SST turbulence model in ANSYS-CFX on an EDPF with a 390 mm diameter shroud dimension, showed a 6.38% increase in thrust at 10,000 rpm compared to the baseline model. This improvement is attributed to enhanced head flow behavior and pressure redistribution within the duct.

Another important aerodynamic characteristic of the eDPF system is in the air intake region, where the airflow encounters significant geometric acceleration and flow separation. The curvature of the duct edge, the angle of the inlet flow, and external turbulence from forward flight all affect the quality of the inlet flow to the rotor. Sun et al. [5] study the aerodynamic behavior of ducted fans under various velocities, angles of attack, and blade loading. Their findings indicate that thrust and power performance are highly sensitive to rotor blade tip clearance and duct length, especially when the angle of attack creates a non-uniform inlet. For example, excessively large head clearance can amplify vortex formation and lead to an unstable thrust region, while excessively long ducts can cause pressure losses due to increased surface friction. These observations are crucial for designing EDFs for practical flight ranges beyond static conditions.

Simulation results must be validated by experiment. Chu et al. [6] perform static tests on a 390 mm eDPF using two battery configurations (8-pack and 9-pack battery). They evaluate thrust, current consumption, rotational speed, and sound emissions of eDPF. They find that aerodynamic performance, measured by the dimensionless figure of merit (FM) is stable between 0.7 and 0.75 at average operating speeds. Their tests show that airflow quality at the rotor intake significantly affects thrust, even when engine input power stays constant.

In addition to single-fan configurations, array-based eDPF deployments, particularly in Distributed Electric Propulsion (DEP) architectures, present challenges regarding aerodynamic turbulence. Dorfling and Traub [7] study the performance of arrays and find that fan spacing and alignment significantly affect total thrust. Narrow spacing leads to congestion and mutual flow distortion at the intake, reduce the ability of each fan to maintain effective intake and exhaust. Such effects must be mitigated in multi-fan systems through the creation of an aerodynamic enclosure or optimal spacing layout strategies.

The aerodynamic flexibility of eDPF also leads to their application in robot mobility. Andrikopoulos and Nikolakopoulos [8] study a Vortex Adhesion System (VAS) in eDPF for wall-climbing robots. The study took advantage of the low-pressure field created beneath the duct to generate suction, enabling vertical adhesion. Their analysis shows that the suction capability depends not only on the fan thrust but also on the duct shape, tip, and flow confinement—all core aerodynamic variables.

Hou et al. [9] make a novel ducted UAV model using Magnus-effect propulsion and show that exhaust stream interaction can generate sufficient lift and stable attitude control. Maintaining aerodynamic stability under complex dynamic conditions is critical to structural integrity. Chung et al. [10] comprehensively evaluate the aerodynamic characteristics of a standard dynamic model in rotational motion. Similarly, Adnan et al. [11] optimize the aerodynamic drag of low-altitude rockets with different wing configurations, and Pua'at et al. [12] study the pressure center shift for different wing configurations, providing insights into vertical stability.

Optimizing internal flow and rotor design is crucial for enhancing overall performance. Faris et al. [13] study a comprehensive review of the application of computational fluid dynamics (CFD) in the design and performance evaluation of UAV propellers. Their research makes the crucial role of

 doi:10.20944/preprints202604.1792.v1

numerical simulation in improving geometric parameters—such as wing shape and twist angle—to achieve optimal aerodynamic efficiency.

To further push the boundaries of aerodynamic performance, particularly by mitigating flow separation and tip clearance leakage losses, various active and passive flow control techniques have been applied. Mao and Liu [14] numerically investigated the impacts of a circumferential single casing groove in a transonic fan rotor. Their results indicated that the groove significantly reduced tip leakage flow intensity and delayed stall inception, thereby improving the safe operating boundary. At the leading edge, Ntantis et al. [15] demonstrated that sinusoidal perturbations effectively delay flow separation and improve lift at high angles of attack. In air intake systems, Khurana et al. [16] successfully utilized air jets to suppress shock-induced separation. Particularly for axial compressors, which share similar physical characteristics with eDPFs, Tran et al. [17] proved that utilizing circumferential bleeding airflow on the casing effectively controls tip leakage flow, increasing the pressure ratio. Building upon this principle, Dinh et al. [18] showed that applying a hybrid inclined groove-recirculation casing treatment successfully manipulates tip leakage flow, significantly improving the stability boundary and overall performance.

The aerodynamic design of EDFs requires a balance between thrust generation, flow stability, and energy efficiency. Using casing grooves, rotor bleeding, optimized duct inlets, and aerodynamic array spacing demonstrates improvements in performance metrics. In this paper, the Reynolds-Averaged Navier-Stokes analysis with the SST k-ω turbulence model is used to investigate the eDPF configurations with the secondary air intakes, focusing on internal flow behavior and aerodynamic performance.

2. Numerical Analysis

2.1. Description eDPF Model

eDPF baseline model

Figure 1 shows a 3D model of an electric ducted propulsion fan used in this study. eDPF has 10 rotor blades (magenta color) and 6 strut blades (green color), enclosed within a shroud and nacelle. The inner diameter of the shroud is 390 mm, and blade tip clearance is 2 mm. The hub (yellow color) houses the electric motor and provides structural support for both the rotor and strut blades. In this study, the rotation speed of the rotor is 6000 rpm with static conditions, and there is no inlet velocity applied at the fan entrance.

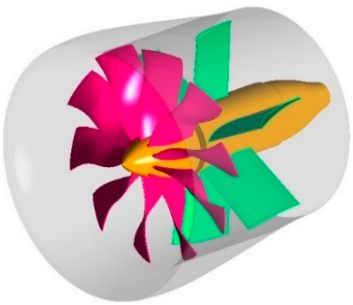

Figure 1. 3D eDPF model.

Figure 2 shows a schematic view and overall dimensions of the model. The nacelle diameter is 458 mm, and the rotor diameter is 390 mm. The blade tip clearance (the gap between the blade tip and the inner surface of the shroud) is 2 mm. The length of the outer duct is 428 mm. The diameter of the rotor hub is 110 mm. A central shaft extends along the axis of the model and connects the rotor cone to the center body. This shaft acts as the mechanical link between the rotating and stationary parts of the eDPF.

 doi:10.20944/preprints202604.1792.v1

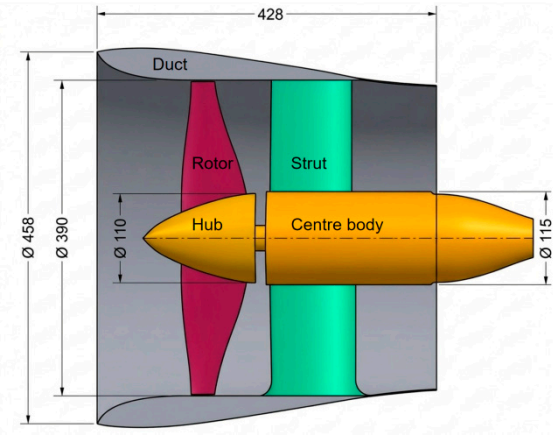

Figure 2. Schematic view and overall dimensions of the eDPF.

2.2. eDPF Model with Secondary Air Intake

We design the air intake channel on the inner surface of the duct wall to add more airflow to the eDPF. This added airflow helps increase the total mass flow into the rotor region and raise the thrust performance of the eDPF. The airflow of the intake channel must not interfere with the main flow path and ensure that engine efficiency remains intact.

To investigate the effect of intake channel geometry on the performance of the eDPF, we use 4 parameters: the axial distance from the rotor trailing edge to the intake outlet (L_{out}/C), curvature radius of the guide surface (R/C), intake inlet width (W_{in}/C), and intake outlet width (W_{out}/C) are illustrated in Figure 3, where C represents the length of the rotor blade chord (30 mm). These parameters define the shape and position of the air flow intake integrated into the duct wall, which directs airflow toward the rotor tip region. In this study, we vary each parameter independently within a defined range, while we hold the others at their reference values listed in Tab. 1. Tab. 2 shows the specific bounds and step sizes used for the parametric sweep. Thrust performance is the main aerodynamic metric used for evaluation and will be compared with the non-intake baseline case to determine the influence of each geometric factor on eDPF efficiency.

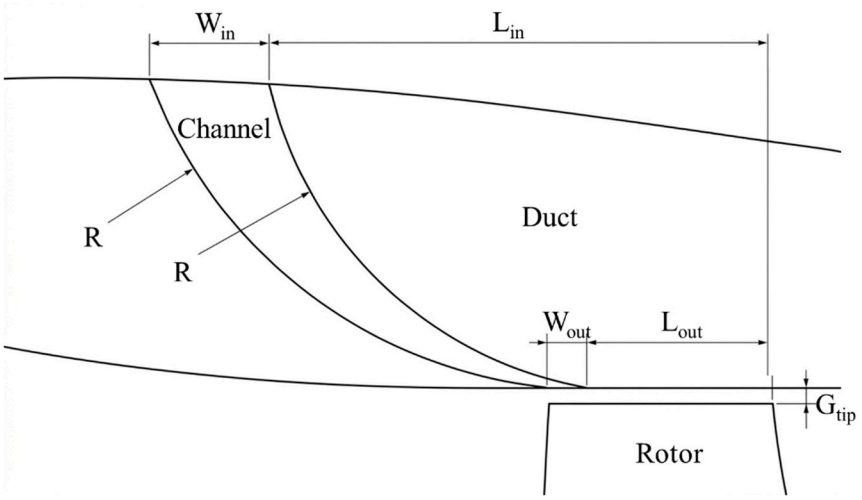

Figure 3. Design of Secondary Air Intake.

Table 1. Dimensionless reference values for the Secondary Air Intake.

Variable	L_{out}/C (%)	R/C (%)	W_{in}/C (%)	W_{out}/C (%)
Reference value	80	200	50	20

 doi:10.20944/preprints202604.1792.v1

Table 2. Dimensionless ranges of parameters for the Secondary Air Intake.

Variable	Lower bound	Upper bound	Step
L_{out}/C (%)	10	150	10
R/C (%)	150	300	50
W_{in}/C (%)	30	60	10
W_{out}/C (%)	10	40	10

2.3. Computational Domain

The computational domain in this study is defined with distances of 5D upstream and 14D downstream from the fan and a radial extent of 5D, where D is the inner diameter of the fan duct, as illustrated in Figure 4. We must make sure this domain size is large enough for the boundary conditions not to be affected by the flow around the eDPF. The simulation domain is divided into two regions: a rotating domain and a stationary domain, as illustrated in Figure 5.

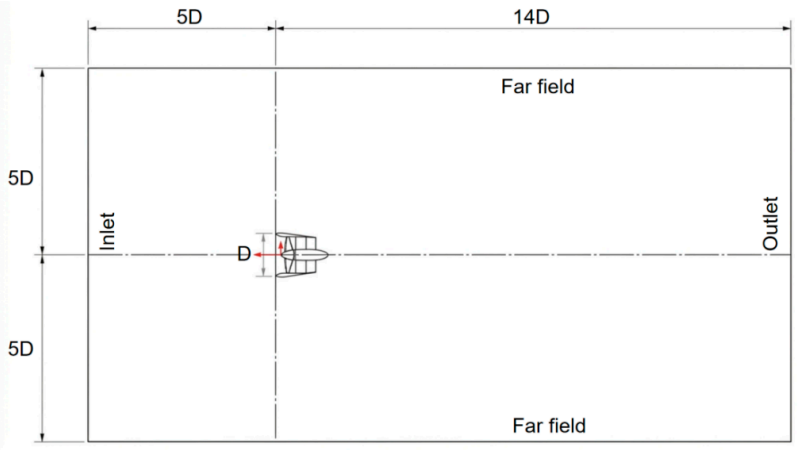

Figure 4. Computational domain.

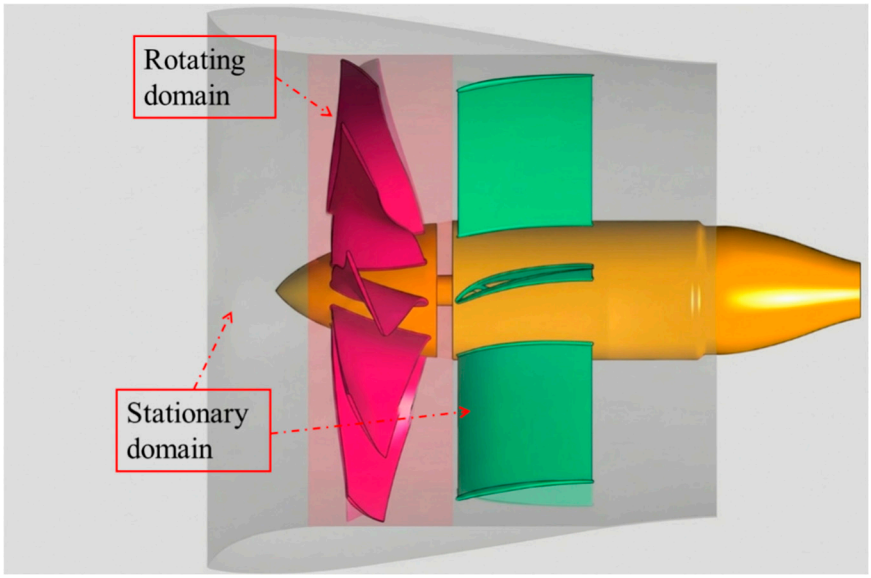

Figure 5. Rotating and stationary domain.

 doi:10.20944/preprints202604.1792.v1

2.4. Meshing

In this study, we use ICEM CFD to create the mesh with the structure of hexhedron elements of eDPF. To optimize computation, the model was divided into different sectors: the rotor is modeled as a 36-degree sector, while the strut, outer domain, and intake channel use a 60-degree sector. This setup offers greater flexibility for geometry modifications and enhances precision in critical areas. To accurately capture the boundary layer near solid walls, the mesh in these regions was highly refined with a first cell height of just $2x10^{-5}$ m and a growth rate of 1.2 to make smooth transitions between all domains. Finally, we generate four types of meshes for independence testing, with the dimensions of each type of mesh being 1.41, 1.93, 3.03, and 4.18 million nodes, respectively.

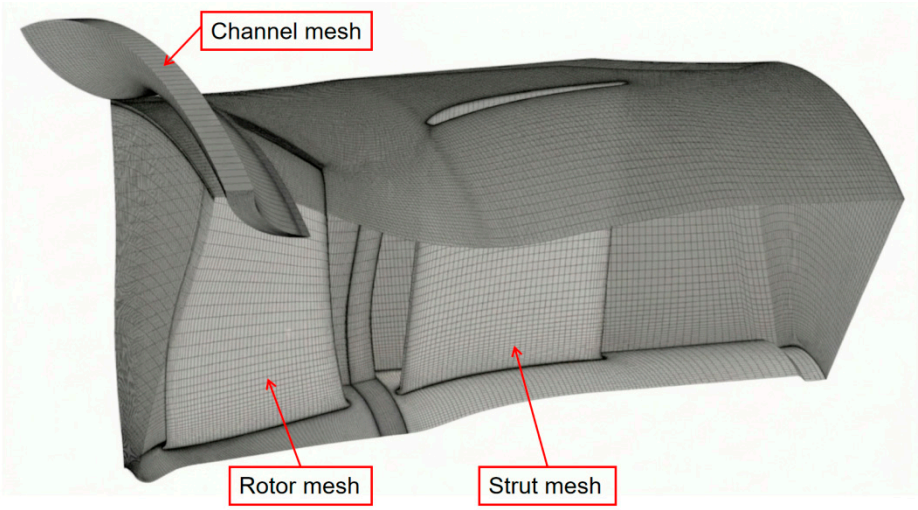

Figure 6. Structural mesh of Rotor, Strut, and intake channel regions.

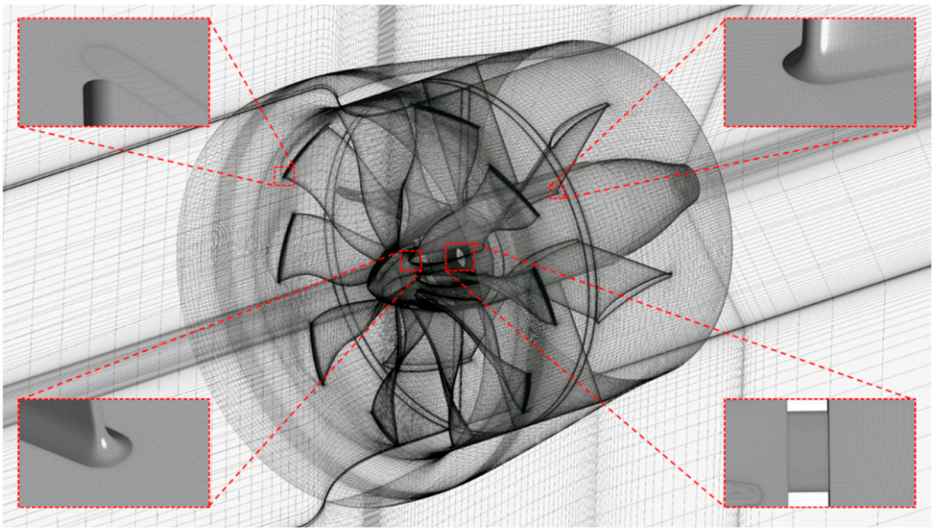

Figure 7. Detailed 3D mesh of the ducted fan computational domain.

Table 3. Grid parameters of different grid configurations.

Nodes number	Mesh#1	Mesh#2	Mesh#3	Mesh#4
Rotor domain	390,612	564,156	1,030,404	1,925,984
Strut and out domain	1,022,563	1,368,715	1,996,049	2,258,391
Total Periodic	1,413,175	1,932,871	3,026,453	4,184,375
Total	10,041,498	13,853,850	22,280,334	22,810,186

 doi:10.20944/preprints202604.1792.v1

2.5. Boundary Conditions

Table 4 summarizes the boundary conditions used in this study. The inlet and outlet are both set to 0 Pa to represent a static environment. The far field is defined as an opening with 0 Pa, allowing flow to enter or exit freely. The rotor domain is set to rotate at 6000 rpm in the counterclockwise direction, while all other domains are stationary. Wall boundaries are set as no-slip and smooth to simulate realistic viscous effects near solid surfaces. The Frozen Rotor interface is used to connect the rotating and stationary regions in a steady-state setup, allowing flow transfer between domains while keeping the relative blade position fixed. Figure 8 shows the detail of the boundary regions in the computational domain.

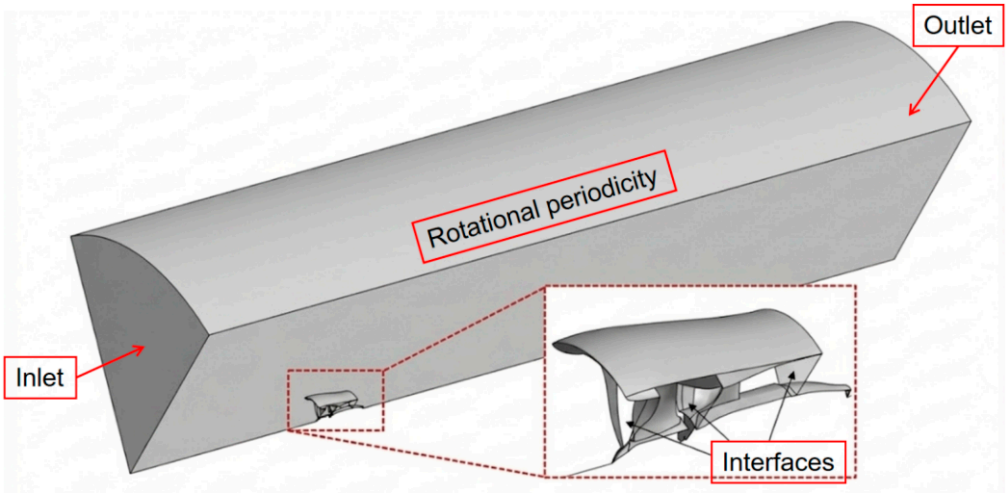

Figure 8. Boundary conditions for periodic mesh configuration.

Table 4. Boundary conditions.

Type	Boundary Condition Settings	Value
Inlet	Total Pressure	0 Pa
Outlet	Average Static Pressure	0 Pa
Interface	General Connection (Frozen Rotor) Rotational Periodicity	N/A
Wall	No Slip Wall, Smooth Wall	N/A
Rotating Domain	Rotating	6000 rpm
Stationary Domain	Stationary	N/A

2.6. Numerical Analysis

This simulation uses the SST k-ω turbulence model. We chose this model because it is highly effective for ducted fans—it accurately predicts how air flows right next to surfaces and handles rapid changes in air pressure without taking too much computing time. To ensure we capture this surface-level airflow perfectly, the mesh around the blades was made extremely fine (achieving low y^+ values).

2.7. Theoretical formulation

In an eDPF system, the total thrust (T_{net}) equals the combined aerodynamic force of the duct (T_{duct}) and the thrust produced by the core (T_{core}) (which includes the fan blade/hub, strut blade/hub, nose, and tailcone):

 doi:10.20944/preprints202604.1792.v1

$$T_{net} = T_{core} + T_{duct}$$

By applying the integral momentum theory, the net thrust is derived as:

$$T_{net} = \dot{m}\,(v_e - v_0) + (P_e - P_a)A_e$$

where $\dot{m}$ is the mass flow rate, v_e and v_0 are the respective exit and freestream velocities, P_e and P_a are the exit and freestream pressure and (A_e) is the exit area.

In this case, $P_e = P_a = 1$atm. So, the net thrust is calculated as follows:

$$T_{net} = \dot{m}\,(v_e - v_0)$$

Flow rate denotes the volume or mass of fluid transported through the propulsion system per unit time. Accordingly, the equation for the mass flow rate is given by:

$$\dot{m} = \rho \cdot v \cdot A$$

where A denotes the cross-sectional area of the duct/flow path (m^2), v is average flow velocity across the cross − section (m/s) and ϱ is fluid density (e.g., standard air density is approximately 1.225 kg/m^3

Establishing the static moment equation for a ducted fan requires evaluating the net aerodynamic moment about its center of gravity (CG):

$$M = T_{net}.D$$

where D is the inner diameter of the fan duct.

3. Results and Disscusion

3.1. Grid Independence Test and Validation

Figure 9 presents the grid independent test result for the baseline, i.e., the case without intake channel. The grid independence was assessed through four mesh configurations created with increasing density: Mesh#1, Mesh#2, Mesh#3, and Mesh#4. When comparing the results, Mesh#3 shows a thrust difference of only 0.01% compared to Mesh#4, and 1.35% and 3.16% related to Mesh#2 and Mesh#1, respectively. The torque variation is also minimal, Mesh#3 indicates a difference of around 0.05% relative to Mesh#4, and 0.33% and 0.73% linked to Mesh#2 and Mesh#1, correspondingly. Finally, Mesh#3 was selected for further simulations as it offers a good trade-off between accuracy and computational efficiency, providing reliable results without the increased cost of a finer mesh. The optimal mesh results show the thrust and torque of 429.3N and 26.3 Nm, respectively. Chu et al. [6] presented the experimental thrust and torque of 421N and 25.9 Nm. The difference between numerical and experimental results for the thrust is 2% and for the torque only 1.5%.

Figure 10 shows the velocity distribution at 99% span in the baseline configuration. In this case, we can see several distinct low-velocity regions. These areas, indicated by darker blue shades, are primarily located near the leading edge of the rotor blade and extend into the tip region. The presence of these low-velocity regions suggests localized separation and recirculation, which typically degrade aerodynamic performance and reduce thrust output.

 doi:10.20944/preprints202604.1792.v1

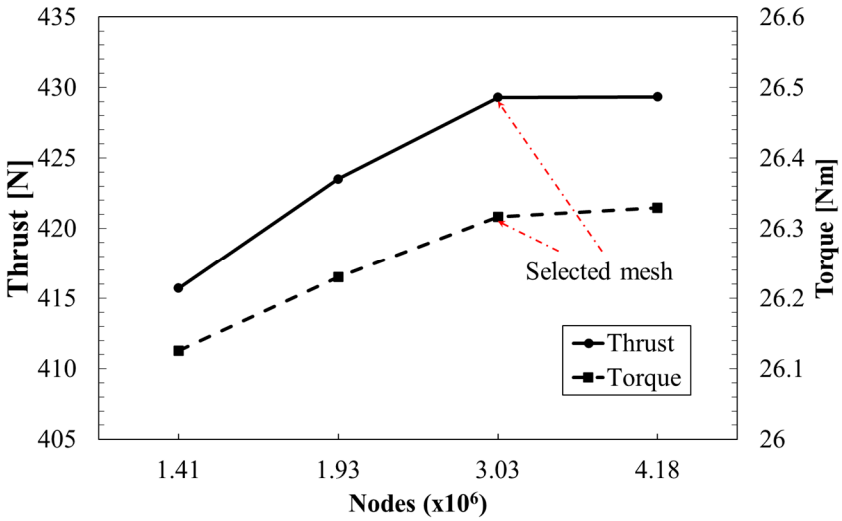

Figure 9. Grid Independence Test.

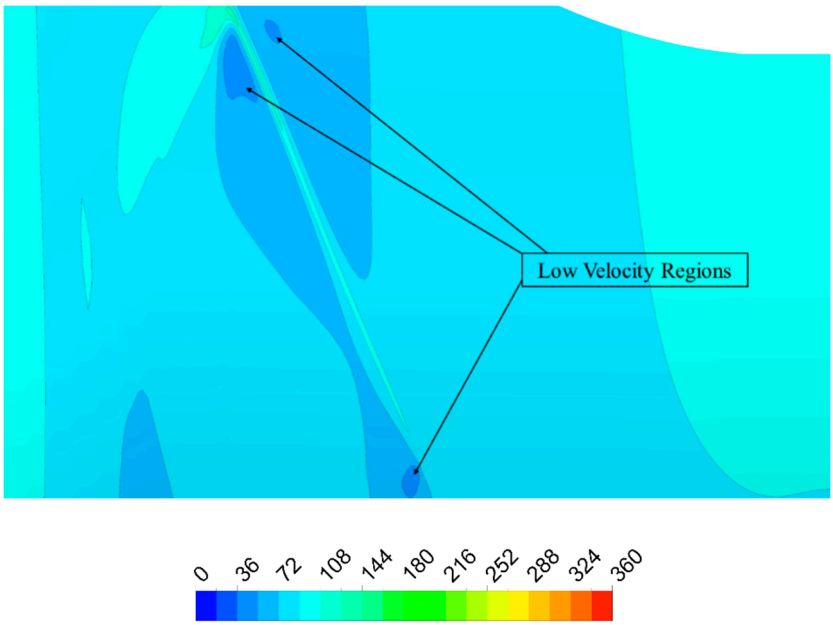

Figure 10. Velocity distribution at 99% span in the baseline configuration.

3.2. Parametric Evaluation of Intake Geometry

To investigate the influence of geometric characteristics of the Secondary Air Intake on the aerodynamic performance of the eDPF, a series of parametric studies was conducted under periodic simulation conditions. The aim was to identify configurations that enhance thrust while minimizing losses and disturbances to the main flow. The intake channel parameters were defined by the following non-dimensional values: outlet position L_{out}/C =80%, curvature radius of the guide surface R/C=200%, inlet width W_{in}/C = 50%, and outlet width W_{out}/C = 20%. Figure 11 shows the grid independent test result for the case with air intake channel, the results explain that the thrust and torque values do not change significantly; however, they still converge to a grid mesh of 38272 nodes. The thrust with the intake channel design enhances to 438.6N as compared to 429.3 N for the case without intake channel. Meanwhile, the torque with the intake channel structure increases very slightly to 26.5 Nm as related to 26.3 Nm for the baseline case.

 doi:10.20944/preprints202604.1792.v1

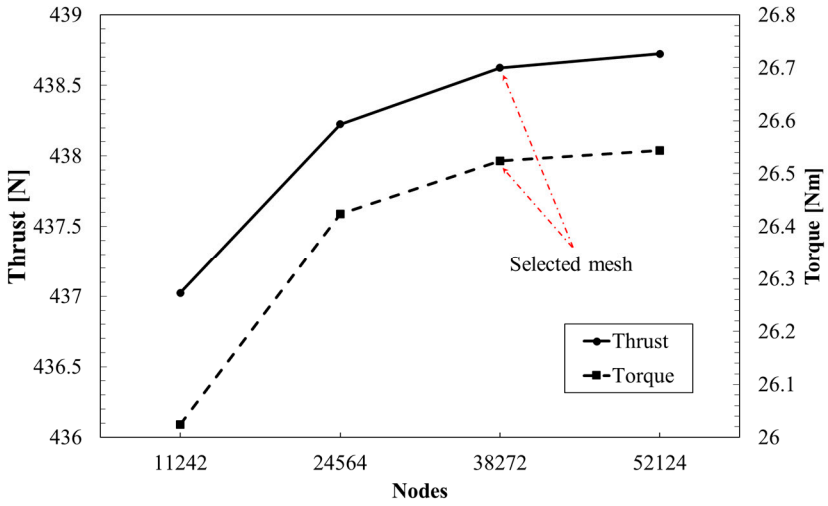

Figure 11. Grid Independence of air intake channel.

By contrast, the curved intake channel configuration (Figure 12) also introduces a high-speed stream into the duct, clearly observed as a bright band near the shroud. However, in this scenario, the reinjected flow is more aligned with the main flow direction, and importantly, the low-velocity zone downstream of the blade tip is significantly reduced or nearly eliminated. This suggests that the curved Intake not only supplies additional mass flow but also facilitates smoother integration with the mainstream, enhancing local flow quality and thrust generation. Removing the low-speed wake enhances pressure recovery and prevents flow separation at the rotor tip. With this aerodynamic baseline established, we now turn to a detailed parametric study of the curved intake geometry.

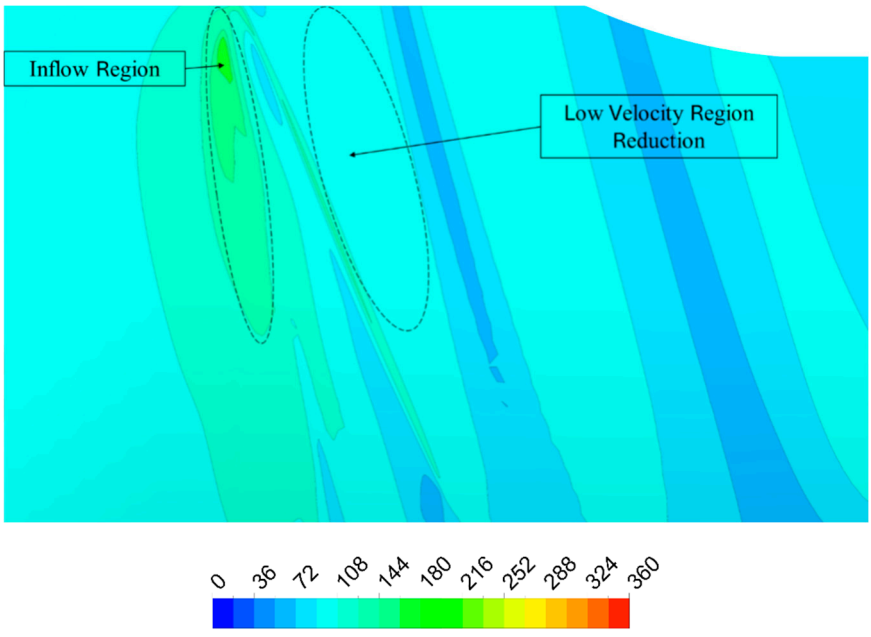

Figure 12. Velocity distribution at 99% span in the curved Intake configuration.

3.3. Geometric Parameter Study of the Air Intake Channel Configuration

Outlet Position L_{out}

The outlet position (L_{out}) measures the distance from the rotor's trailing edge to the intake exhaust, relative to the chord length (C). It controls the reinjection location, fundamentally shaping how the bypass air merges with the primary flow at the rotor tip.

 doi:10.20944/preprints202604.1792.v1

Figure 13 plots the L_{out}/C variations from 10% to 150% in 10% steps. The 80% chord position acts as the baseline because it provides the best balance for flow integration, ensuring the reinjected air joins the mainstream without disrupting the trailing-edge aerodynamics.

Against the no-intake baseline configuration as shown in Figures 13 and 14, shifting the outlet between 10% and 120% chord length led to stable aerodynamic gains, maximizing thrust at 80% by the smooth flow integration. However, an outlet positioned at 130% or beyond makes a massive performance penalty. Thrust drops sharply from 438.6 N to 325.8 N, and torque falls to 21.9 Nm. This proves that placing the outlet too far downstream severely disrupts the rotor wake and triggers heavy flow separation, ruining propulsion efficiency

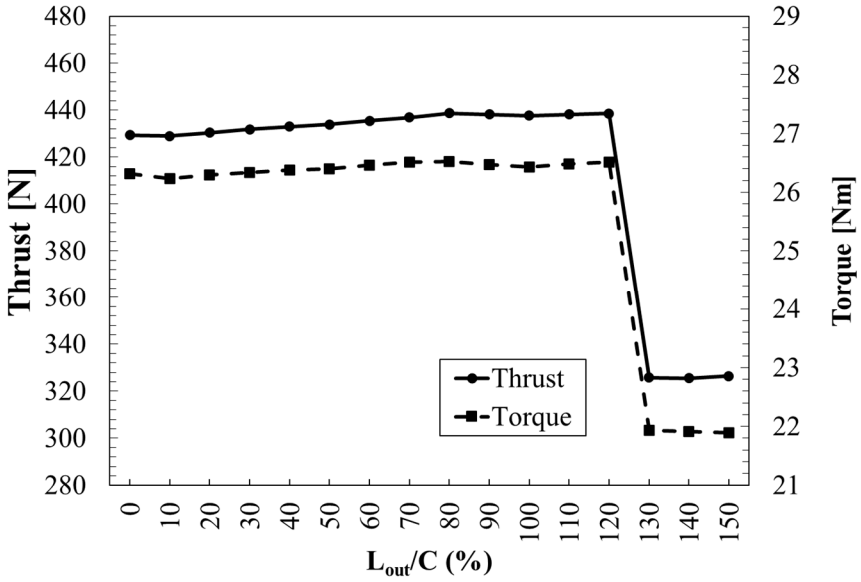

Figure 13. Thrust and Torque versus Outlet Position (10–150% Chord Length).

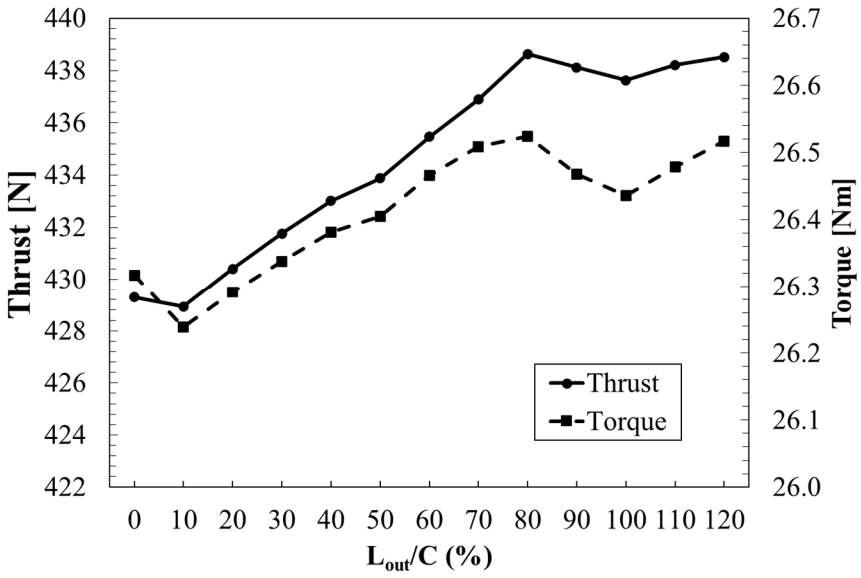

Figure 14. Thrust and Torque versus Outlet Position (10–120% Chord Length).

In the L_{out}/C = 130% case (Figures 15 and 16), Excessive downstream outlet placement relative to the rotor trailing edge, causing the reinjected flow to detach from the inner hub surface and curve abruptly into the duct. Spanwise and streamwise contours reveal that this misalignment induces a large-scale vortex via the interaction between the reinjected jet and the pre-existing low-velocity zone

 doi:10.20944/preprints202604.1792.v1

ahead of the outlet. This vortex blocks the flow zone near the blade tip, limiting the core flow's development and reducing aerodynamic effectiveness. Thus, thrust drops sharply due to increased separation and energy loss.

In the L_{out}/C = 120% scenario, the outlet is positioned slightly closer to the rotor compared to previous case, i.e., 130%, allowing the reinjected flow to better align with the duct wall. While the contours show better bypass-to-mainstream integration and weaker recirculation, some flow diffusion and energy loss persist in the streamwise plane. Consequently, this setup yields only moderate performance improvements rather than optimal aerodynamic efficiency.

The 80% chord outlet position achieves the most effective flow reinjection. Its tangential entry along the duct surface re-energizes the tip flow without causing downstream disturbances. Cross-sectional data shows a highly streamlined flow with minimal separation and reduced wake regions. Consequently, this configuration generates the highest thrust among all tested cases, making it the optimal aerodynamic choice.

In the L_{out}/C = 50% case, placing the outlet so close to the trailing edge restricts the flow's development length. Consequently, the reinjected air turns sharply and mixes poorly, leaving local disturbances and low-velocity zones near the blade tip. Although it beats the 130% setup, its true potential is hindered by an inefficient injection trajectory and premature wake interaction.

As demonstrated, locating the outlet at 80% chord maximizes aerodynamic efficiency through smooth flow reinjection and reduced mainstream interference. Given these clear physical benefits, this position serves as the reference geometry for the remainder of our parametric investigations.

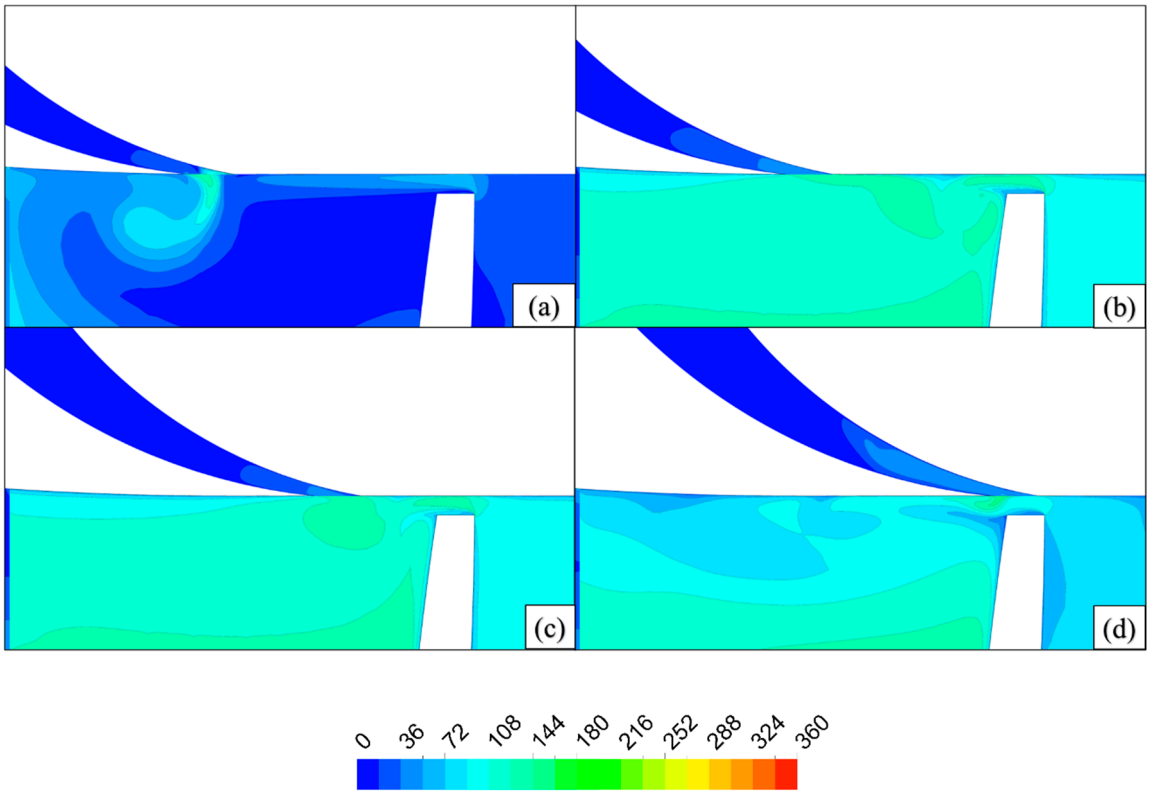

Figure 15. Velocity contour near blade tip: (a) Case L_{out}/C = 130%, (b) Case L_{out}/C = 120%, (c) Case L_{out}/C = 80%, (d) Case L_{out}/C = 50%.

 doi:10.20944/preprints202604.1792.v1

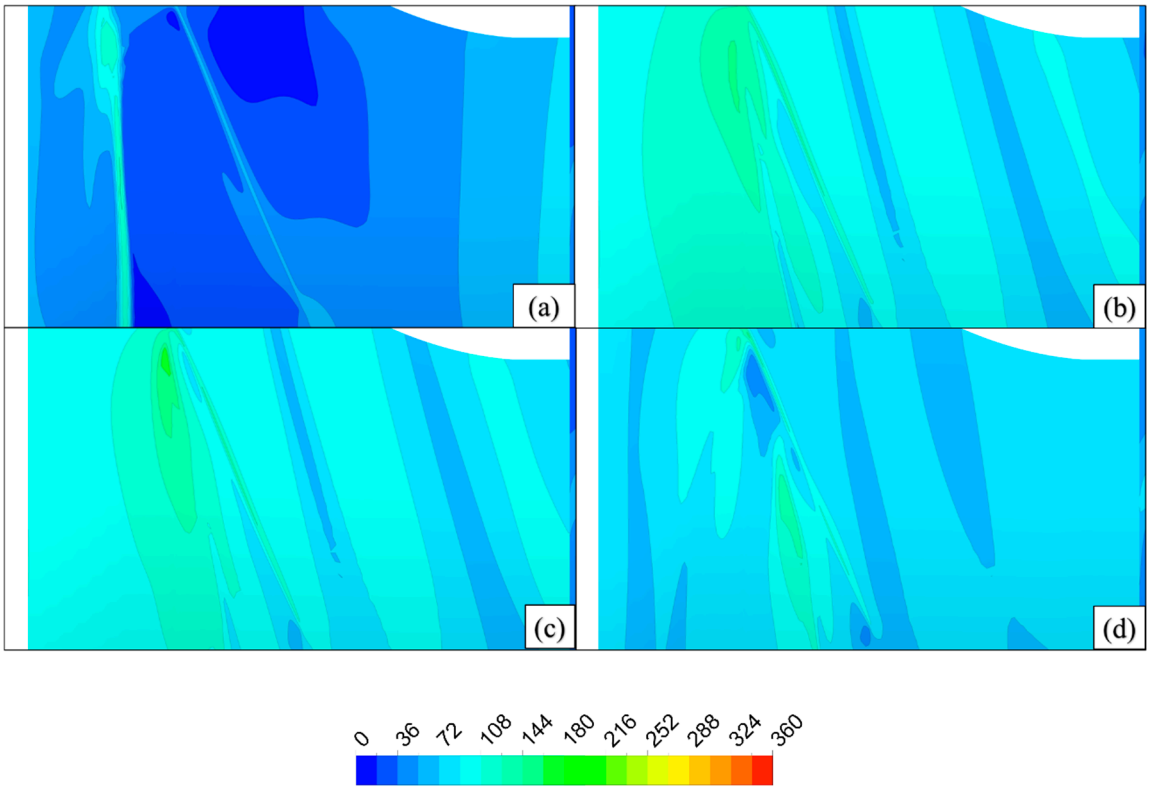

Figure 16. Velocity distribution at 99% span: (a) Case L_{out}/C = 130%, (b) Case L_{out}/C = 120%, (c) Case L_{out}/C = 80%, (d) Case L_{out}/C = 50%.

Radius of Curvature R

We also investigated the air intake channel radius of curvature (R), which controls how well the bypass flow integrates with the mainstream to prevent separation. Against the no-intake baseline (Figure 17), a tight 150% C radius restricts performance to a minimum (355 N thrust, 23 Nm torque). Broadening the radius to 200% resolves the issue, pushing thrust to a peak of 440 N. Any further expansion up to 300% simply results in a performance that remains unchanged. Therefore, an R/C of 200% is the system's aerodynamic optimize point, capturing maximum thrust benefits.

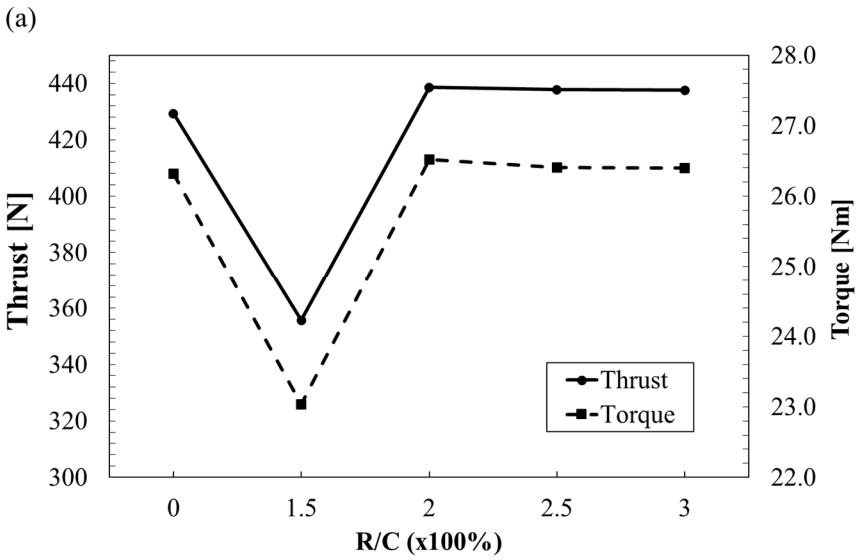

 doi:10.20944/preprints202604.1792.v1

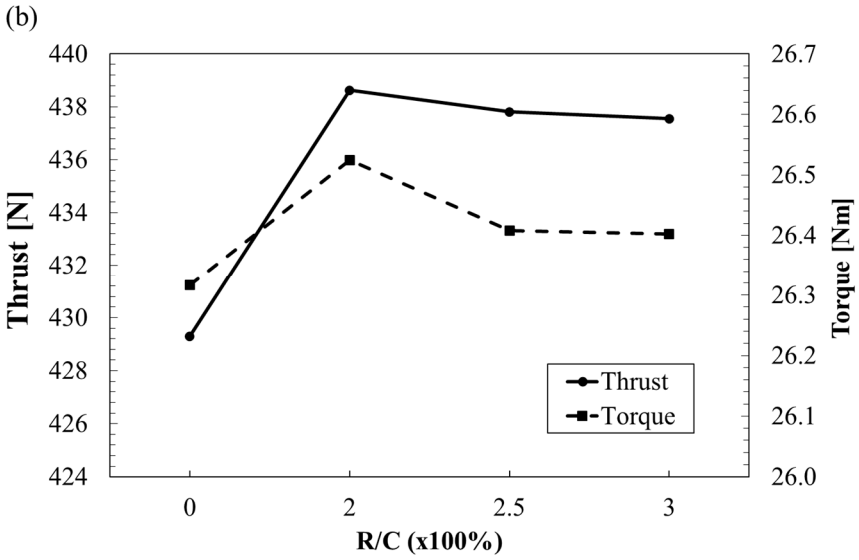

Figure 17. Thrust and Torque versus Radius of Curvature.

The effect of the radius of curvature R on flowfield characteristics is clearly illustrated in the velocity contours near the blade tip, as displayed in Figure 18. The R/C=150% design suffers from overly aggressive curvature, which forces the bypass flow out of alignment with the mainstream. This triggers a large recirculation zone ahead of the outlet. Ultimately, this vortex creates a flow blockage at the rotor tip, leading to a significant thrust penalty.

In contrast, velocity contours in Figures 18 and 19 confirm that the R/C=200% geometry delivers optimal aerodynamics. The moderate curvature ensures the bypass flow integrates cleanly with the mainstream, bypassing the massive recirculation and separation issues found at R/C=150%. This smooth, high-velocity flow over the blade tips is directly responsible for the maximum thrust achieved. Therefore, R/C=200% serves as the baseline curvature for all following investigations.

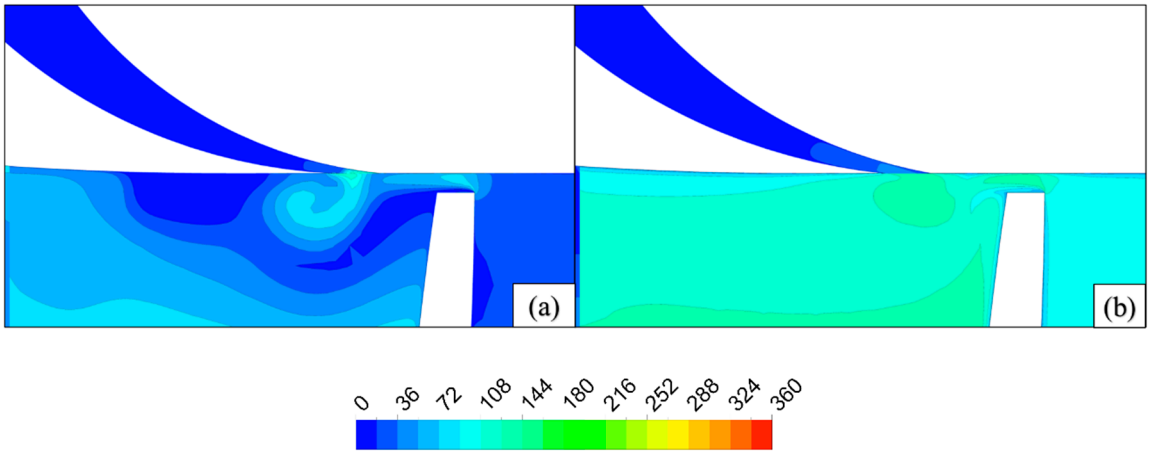

Figure 18. Velocity contour near blade tip: (a) Case R/C=150%, (b) Case R/C=200%.

 doi:10.20944/preprints202604.1792.v1

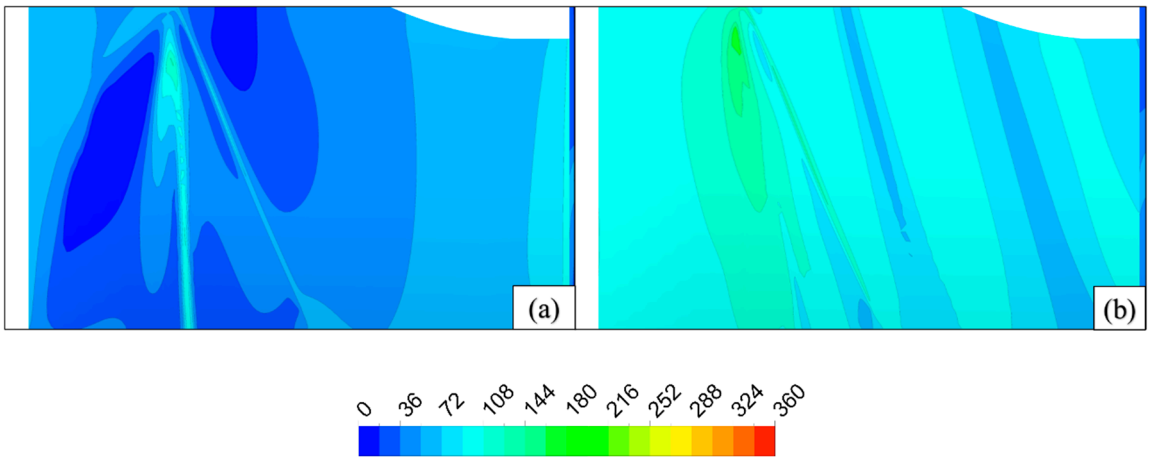

Figure 19. Velocity distribution at 99% span: (a) Case R/C=150%, (b) Case R/C=200%.

Inlet Width W_{in}

Next, to analyze the geometry of the air intake channel, we examine the inlet width (Win). This parameter governs the bypass entry area and the resulting amount of reinjected air. A wider inlet pulls in more mass flow, directly enhancing the aerodynamic efficiency near the rotor tip. In this study, the outlet position is fixed at 80% chord, and the outlet width is kept at 20% - values selected from the reference case. The inlet width varies from 30% to 60% of C.

As illustrated in Figure 20, the plotted results show a relatively flat trend in both performance metrics across the tested range and the condition of $W_{in}/C = 0\%$ is the result of the case without an air intake channel. Thrust slightly increases from 438.4 N at 30% and peaks at 50% with a magnitude of 438.6 N and drops to 438.3 N at 60%, while torque decreases steadily from 26.6 Nm at 30% to 26.5 Nm at 60%. However, the overall variation in performance is minimal, with thrust and torque fluctuating by less than 0.5 N and 0.1Nm, individually. Therefore, based on the observations from Figure 21, the inlet width is identified as the least influential geometric parameter among those investigated. The final configuration locks this dimension at 50% to ensure the best balance between a consistent performance peak and compatibility with prior optimizations.

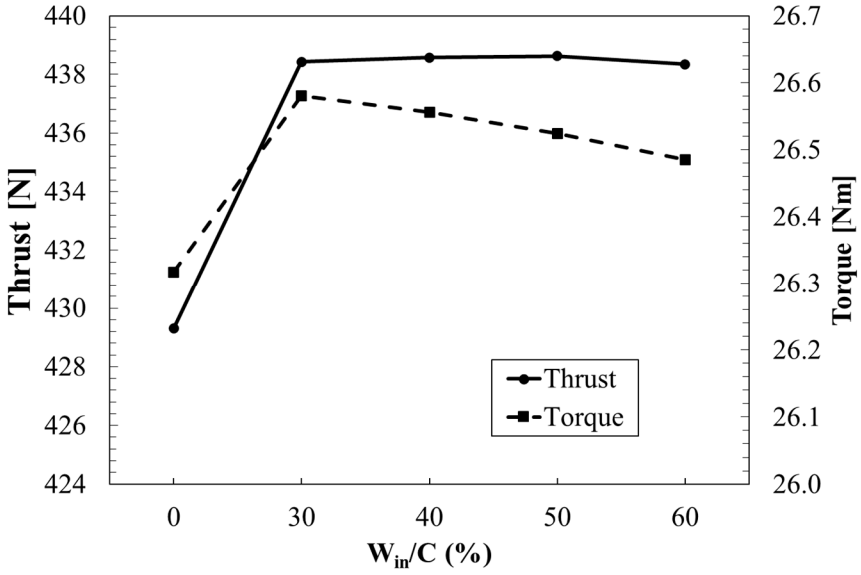

Figure 20. Thrust and Torque versus Inlet Width.

 doi:10.20944/preprints202604.1792.v1

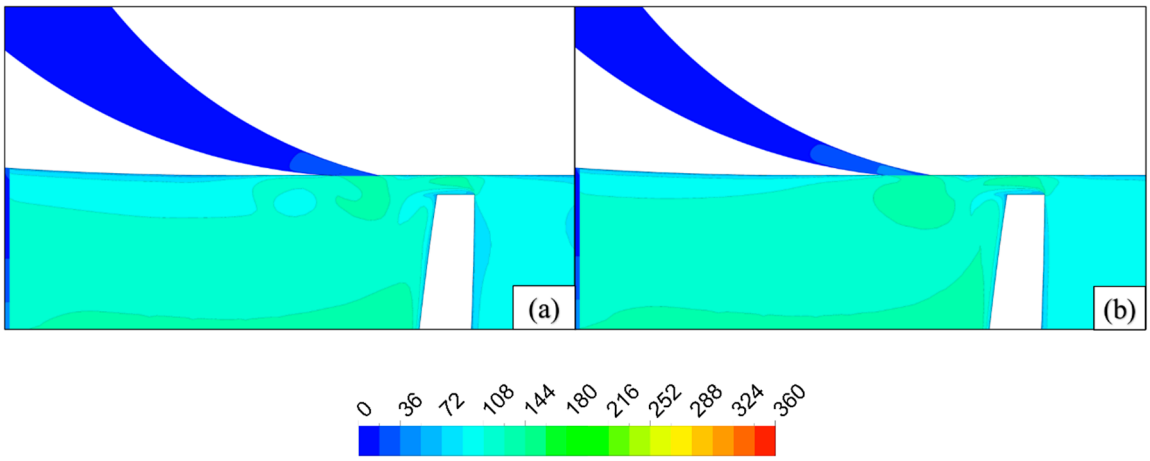

Figure 21. Velocity contour near blade tip: (a) Case W_{in}/C=60%, (B) Case W_{in}/C=50%.

Outlet Width W_{out}

To establish the optimal outlet location, we next analyze the outlet width (W_{out}). This dimension controls the reinjected mass flow, heavily impacting the rotor tip flow dynamics and overall performance. While wider outlets boost injected volume, they risk mainstream interference; conversely, narrow outlets limit potential aerodynamic gains. To capture this trade-off, we performed simulations across widths from 10% to 40% of the chord, keeping the position fixed at 80%.

The effect of outlet width on thrust and torque is detailed in Figure 22. Starting from the baseline case with no intake (W_{in}/C = 0%), thrust improves as the outlet width increases. It reaches an optimal peak at 20% chord, but any further increase in width leads to a gradual loss of thrust. The torque follows a similar trend but with a more consistent downward slope. This trend suggests that while increasing the outlet width initially enhances the flow reinjection and improves propulsive force. Beyond a certain point, the added mass flow starts to interfere with the mainstream, reducing aerodynamic efficiency. The simulations in this study were conducted with outlet widths ranging from 10% to 40% of the rotor chord based on the parameter table.

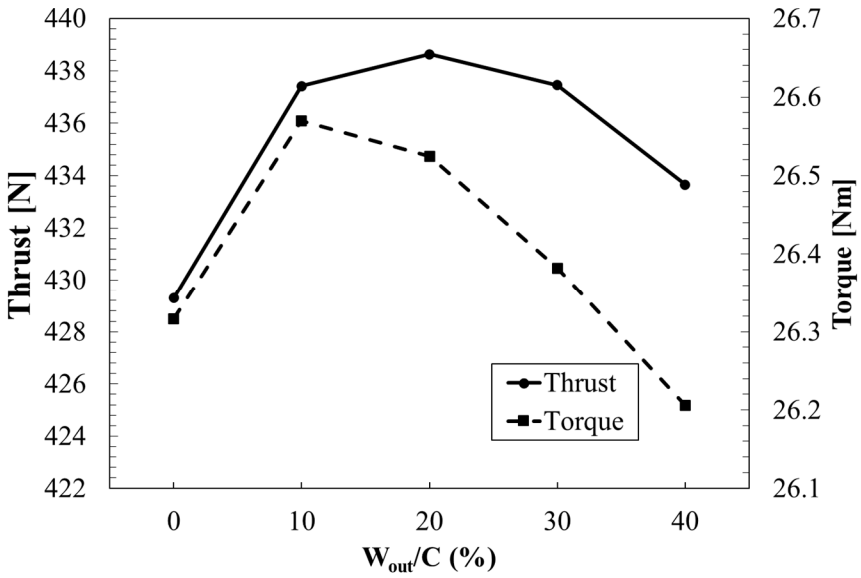

Figure 22. Thrust and Torque versus Outlet Width.

Figure 23 illustrates the velocity contours for 2 case W_{out}/C=40% and W_{out}/C=20%. The 40% model shows a dispersed reinjected flow that quickly separates from the duct, leaving a wide low-velocity

 doi:10.20944/preprints202604.1792.v1

area near the rotor tip. In contrast, the 20% configuration delivers the highest thrust by keeping the reinjected stream tight and aligned with the duct wall. This reduces flow interference and enhances local acceleration at the tip. These flow fields confirm that a 20% chord outlet width provides the ideal compromise between flow reinforcement and stability.

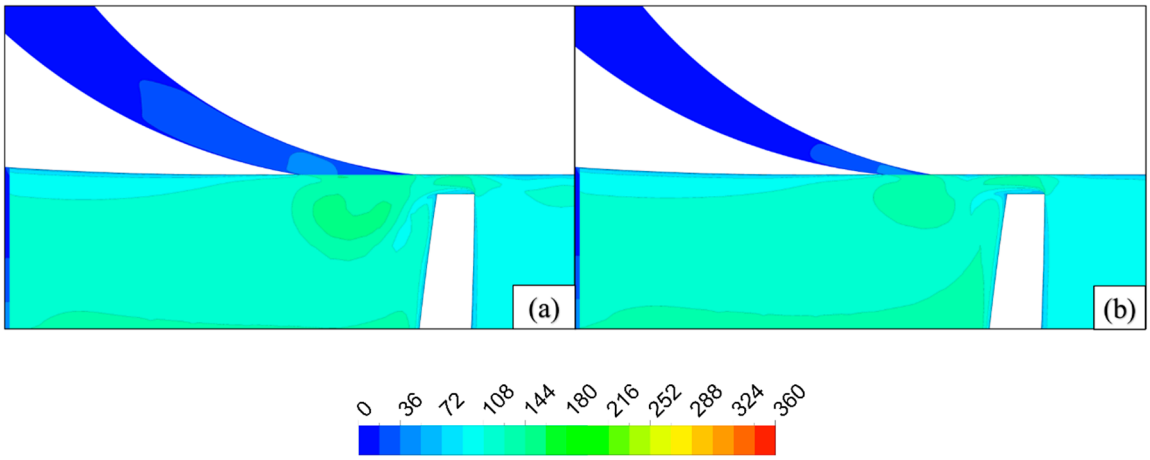

Figure 23. Velocity contour near blade tip. (a) Case W_{out}/C=40%, (b) Case W_{out}/C=20%.

4. Conclusions

This research study the aerodynamic efficiency of an electric ducted propulsion fan featuring a curved intake channel. The study uses 3D CFD simulations to show the bypass flow through a circumferential air intake channel can significantly reduce tip vortex losses, minimize low-velocity zones adjacent to the rotor tip, and improve overall thrust generation. The curved intake channel configuration shows greater flow integration and performance enhancement than the other design variations, which included the baseline and straight intake channel.

In this study, we investigate the geometric parameters of the secondary air intake channel, which is a curved intake, including outlet position, outlet width, curvature radius R, and inlet width. The outlet is positioned at 80% of the rotor chord length, an outlet width of 20% of the chord, a curvature radius of 200% of the chord, and an inlet width of 50% of the chord and was found to deliver optimal aerodynamic performance, increasing thrust by over 2.2% compared to the baseline. Velocity contour analysis shows that these optimized settings greatly smoothed the flow and reduced the size of wake regions.

This study provides stronger aerodynamic benefits of curved air intake channels than the baseline case or other air intake channel configurations. In further study of this air intake channel, we will see how to expand inflow condition modeling to be more effective and optimize the intake channel design. These studies contribute to the advancement of high-performance, low-drag, and less noisy electric ducted propulsion systems for next-generation aircraft.

Author Contributions: Conceptualization, T.S.V. and C.T.D.; methodology, T.S.V. and B.N.N.; software ANSYS, ANSYS CFX 2025 R1, C.T.D. and B.N.N.; validation, B.N.N, H.Q.C., G.D.P. and C.T.D.; formal analysis, T.S.V.; investigation, T.S.V., B.N.N. and H.Q.C.; resources, C.T.D.; data curation, T.S.V.; writing—original draft preparation, T.S.V, B.N.N., H.Q.C. and C.T.D.; writing—review and editing, G.D.P. and C.T.D.; visualization, T.S.V and G.D.P.; supervision, C.T.D.; project administration, G.D.P. and C.T.D.; funding acquisition, C.T.D. All authors have read and agreed to the published version of the manuscript.

Funding: This research is funded by the Vietnam National Foundation for Science and Technology Development (NAFOSTED) through research grant NCUD.02-2023.20.

Institutional Review Board Statement: Not applicable.

Informed Consent Statement: Not applicable.

 doi:10.20944/preprints202604.1792.v1

Data Availability Statement: The original contributions presented in this study are included in the article. Further inquiries can be directed to the corresponding author.

Conflicts of Interest: The authors declare no conflict of interest.

Abbreviations

CFD	Computational Fluid Dynamics
DEF	Distributed Electric Propulsion
eDPF	Electric Ducted Propulsion Fan
eVTOL	Electric Vertical Take-Off and Landing
PAM	Personal Air Mobility
RANS	Reynolds Averaged Navier-Stokes
SST $k-\omega$	Shear Stress Transport $k-\omega$ turbulence model
UAV	Unmanned Aerial Vehicle
Symbols	
C	Rotor blade chord length (mm)
D	Inner diameter of the fan duct (mm)
L_{out}	Axial distance from the rotor trailing edge to the Intake outlet (mm)
M	Moment (N.m)
R	Curvature radius of the guide surface (degree)
T	Thrust (N)
W_{in}	Intake inlet width (mm)
W_{out}	Intake outlet width (mm)
y^+	Dimensionless wall distance

References

1. Abrego, A.I. and Bulaga, R.W. Performance Study of a Ducted Fan System. American Helicopter Society Aerodynamics, Acoustics and Test and Evaluation Technical Specialists Meeting, San Francisco, Jan. 2002.
2. Dinh, C.T., Heo, M.W. and Kim, K.Y. Aerodynamic Performance of Transonic Axial Compressor with a Casing Groove Combined with Blade Tip Injection. Aerospace Science and Technology, Vol. 43, 2015, pp. 176-187. https://doi.org/10.1016/j.ast.2015.07.006.
3. Dinh, C.T., Vu, D.Q. and Kim, K.Y. Effects of Rotor Bleeding Airflow on Aerodynamic and Structure Performances of Single-Stage Transonic Axial Compressor. Aerospace Science and Technology, Vol. 21, No. 3, 2020, pp. 599-611. https://doi.org/10.1007/s42405-019-00239-5.
4. Vu, T.S., Ha, D.T., Nguyen, Q.V., Pham, G.D. and Dinh, C.T. Aerodynamic Characteristics of an Electric Propulsion Ducted Fan with a Rotor Shroud Air Bleeding Channel. Proceeding of the 4th Annual International Conference on Material, Machines, and Methods for Sustainable Development (MMMS2024), Vol. 1, 2025, pp. 431-438.
5. Sun, L., Liu, X., Tao, Q. and Yang, J. Aerodynamic Performance of Ducted fans for Large-scale Electric Propulsion Aircraft under Variable Operating Conditions. Physics of Fluids, Vol. 37, No. 2, 2025. https://doi.org/10.1063/5.0260520.
6. Chu, H.Q., Dinh, Q.N., Vu, T.S., Pham, V.Y., Bui, V.T., Hoang, N.M., Nguyen, T.K., Nguyen, D., Pham, G.D. and Dinh, C.T. Static Aero-Propulsion Experiment of an Electric Ducted Fan. Aerospace, Vol. 12, No. 509, 2025. https://doi.org/10.3390/aerospace12060509.
7. Dorfling, J. and Traub, L.W. An Experimental Study of the Performance of Ducted Fan Arrays for Distributed Electric Propulsion. AIAA Journals, 2023. https://doi.org/10.2514/6.2023-4047.
8. Andrikopoulos, G. and Nikolakopoulos, G. Vortex Actuation via Electric Ducted Fan: an Experimental Study. Journal of Intelligent & Robotic Systems, Vol. 95, 2019, pp. 955-973. https://doi.org/10.1007/s10846-018-0925-2.
9. Hou, Q., Zhao, J., Zhu, Y., Li, G. and Jin, H. A Novel Ducted-Fan UAV Model Using Magnus Effect Steering Engine. Journal of Aeronautics, Astronautics and Aviation, Vol. 46, No. 3, 2014, pp. 209-217. https://doi.org/10.6125/13-0901-760.

 doi:10.20944/preprints202604.1792.v1

10. Chung, K.M., Huang, Y.X., Chen, W.H., Liao, Y.T. and Huang, J.M. Aerodynamic Characteristics of a Standard Dynamics Model in a Spinning Motion. Journal of Aeronautics, Astronautics and Aviation, Vol. 54, No. 2, 2022, pp. 215-226. https://doi.org/10.6125/JoAAA.202206_54(2).07.
11. Adnan, A.A., Hamid, A.H.A., Salleh, Z. and Azizi, M.Z. Mathematical and Computational Fluid Dynamics Analysis of Low-Altitude Rocket Drag for Various Fin Configurations. Journal of Aeronautics, Astronautics and Aviation, Vol. 56, No. 3, 2024, pp. 781-790. https://doi.org/10.6125/JoAAA.202407_56(3).12.
12. Pua'at, A.A., Zhahir, A., Hamid, M.F.A., Gires, E., Ahmad, M.T. and Hassan, A. Investigation on the centre of pressure migration for different wing configurations. Journal of Aeronautics, Astronautics and Aviation, Vol. 54, No. 3, 2022, pp. 261-271. https://doi.org/10.6125/JoAAA.202209_54(3).03.
13. Faris, A.F.A., Basri, A.A., Basri, E.I., Gires, E., Sultan, M.T.H. and Ahmad, K.A. Propeller Design and Performance Evaluation by Using Computational Fluid Dynamics (CFD): A Review. Journal of Aeronautics, Astronautics and Aviation, Vol. 53, No. 2, 2021, pp. 263-274. https://doi.org/10.6125/JoAAA.202106_53(2).19.
14. Mao, X. and Liu, B. Numerical Investigation of the Impacts of Circumferential Single Casing Groove Location on the Overall Performance in a Transonic Fan Rotor. Journal of Aeronautics, Astronautics and Aviation, Vol. 51, No. 3, 2019, pp. 249-264. https://doi.org/10.6125/JoAAA.201909_51(3).03.
15. Ntantis, E.L., Francis, E., Pugazendi, V., George, J., Tarek, A., Emthias, M. and Rasheed, S. Study of Sinusoidal Perturbations on the Leading Edge of an Aircraft Wing. Journal of Aeronautics, Astronautics and Aviation, Vol. 53, No. 3, 2021, pp. 375-386. https://doi.org/10.6125/JoAAA.202109_53(3).04.
16. Khurana, S., Gahloy, N.K. and Singh, N.K. Numerical Simulation of Air Jet Effects on Shock-induced Separation Control in Mixed Compression Supersonic Air Intake. Journal of Aeronautics, Astronautics and Aviation, Vol. 57, No. 1, 2025, pp. 29-39. https://doi.org/10.6125/JoAAA.202501.
17. Tran, D.Q., Le, X.T., Nguyen, V.H., Dinh, C.T. and Vu, T.S. Aerodynamic Performance Optimization of a Single-stage Axial Compressor using Circumferential Bleeding Airflow. Journal of Aeronautics, Astronautics and Aviation, Vol. 54, No. 4, 2022, pp. 451-466. https://doi.org/10.6125/JoAAA.202212_54(4).07.
18. Dinh, C.T., Nguyen, V.H., Tran, D.Q., Vu, T.S., Nguyen, C.T. and Bui, X.L. Aerodynamic Performance of a Single-stage Transonic Axial Compressor using a Hybrid Inclined Groove-Recirculation Casing Treatment. Journal of Aeronautics, Astronautics and Aviation, Vol. 55, No. 2, 2023, pp. 143-157. https://doi.org/10.6125/JoAAA.202306_55(2).04.